Journal of Materials Chemistry C

PAPER

View Article Online
View Journal | View Issue

Cite this: J. Mater. Chem. C, 2016, 4, 4792

Hysteretic magnetoelectric behavior of $CoFe_2O_4$–$BaTiO_3$ composites prepared by reductive sintering and reoxidation

Till Walther,[a] Ulrich Straube,[b] Roberto Köferstein[a] and Stefan G. Ebbinghaus*[a]

Received 8th March 2016,
Accepted 14th April 2016

DOI: 10.1039/c6tc00995f

www.rsc.org/MaterialsC

Magnetoelectric composites $(CoFe_2O_4)_x$–$(BaTiO_3)_{1-x}$ with x = 0.1, 0.2, 0.3, 0.4 and 0.5 were prepared by a polyol mediated synthesis route. The densification step was performed in a reducing forming gas atmosphere at 1250 °C. Under these conditions Co^{2+} and Fe^{3+} are reduced to the corresponding metals and thus a reaction of these elements with the $BaTiO_3$ matrix is prevented. Reoxidation in air to $CoFe_2O_4$ at a rather low temperature of 800 °C leads to samples free of secondary phases. While the course of the synthesis was monitored by TGA, XRD and photometric analysis, the final composites were characterized *via* SEM, EDX, impedance spectroscopy and magnetic and magnetoelectric (ME) measurements. All samples show pronounced ME hystereses and α_{ME} maxima dependent on the H_{dc} field sweep direction. The sample with x = 0.4 exhibits the highest maximum α_{ME} of 420 μV Oe^{-1} cm^{-1}.

1. Introduction

Multiferroic composites consist of a combination of compounds, which exhibit at least one ferroic order phenomenon like ferroelectricity and ferro- or ferrimagnetism. The coupling between magnetostrictive and piezoelectric phases allows manipulating the electric polarization by a magnetic field or the magnetization by an electric field. These so-called direct and indirect magnetoelectric (ME) effects promise new applications and devices, such as spintronics and MERAMS.[1–4] Several composites have been identified as magnetoelectric materials.[5] The first discovered magnetoelectric composite – and still one of the most prominent combinations – is the system consisting of $CoFe_2O_4$ (CFO) and $BaTiO_3$ (BTO).[6] The hard ferrimagnetic $CoFe_2O_4$ shows large magnetostriction while $BaTiO_3$ is ferroelectric with high piezoelectricity. Furthermore, this system is free of resource-critical elements and is predicted to exhibit high ME voltages.[7–10] $CoFe_2O_4$ and $BaTiO_3$ have already been combined in all three prominent connectivities for composite multiferroics, namely 0–3, 1–3 and 2–2.[11,12] The reported α_{ME} values for 0–3 composites are typically ranging from a few μV Oe^{-1} cm^{-1} to 10 mV Oe^{-1} cm^{-1}.[13–15] However, the theoretically predicted much higher α_{ME} values have not yet been achieved.[16] This is most often explained by an insufficient interface between the piezoelectric and magnetostrictive phase that prevents mechanical transfers and thus good coupling. One approach to tailor the interface is to build up composites from nanoparticles because of their large surface to volume ratio. One disadvantage of this strategy is that impurities which originate from the reaction of $BaTiO_3$ with $CoFe_2O_4$ at the interface, like substituted barium hexaferrite $Ba(Co_{0.5}Ti_{0.5})_xFe_{12-x}O_{19}$, are favored by large interface areas. While pure $BaFe_{12}O_{19}$ is multiferroic on its own[17,18] and even composites with perovskites have been investigated,[19,20] the incorporation of Co^{2+} and Ti^{4+} in $BaFe_{12}O_{19}$ has a significant impact on its magnetic properties.[21,22]

To overcome the formation of impurity phases, we present in this article a polyol mediated synthesis route for magnetoelectric $CoFe_2O_4$–$BaTiO_3$ composite ceramics. Using a reductive sintering step followed by reoxidation under mild conditions, the formation of $Ba(Co_{0.5}Ti_{0.5})_xFe_{12-x}O_{19}$ was successfully suppressed and phase pure samples with relative densities >80% were obtained. Measurements of the magnetoelectric coupling show frequency independent values of the ME coefficient above 300 Hz. All samples exhibit a pronounced ME hysteresis with a maximum of α_{ME} at $H_{dc} \approx \pm 2500$ Oe. Furthermore, we for the first time describe a dependence of the maximum α_{ME} values on the direction of the DC-field sweep.

2. Experimental

2.1 Material preparation

All chemicals were used as purchased without further purification, if not stated otherwise. Five samples of $(CoFe_2O_4)_x$–$(BaTiO_3)_{(1-x)}$

[a] Institute of Chemistry, Inorganic Chemistry, Martin Luther University Halle-Wittenberg, Kurt Mothes Strasse 2, 06120 Halle, Germany. E-mail: stefan.ebbinghaus@chemie.uni-halle.de; Fax: +49-345-5527028; Tel: +49-345-5525870

[b] Institute of Physics, Martin Luther University Halle-Wittenberg, von Danckelmann Platz 3, 06120 Halle, Germany

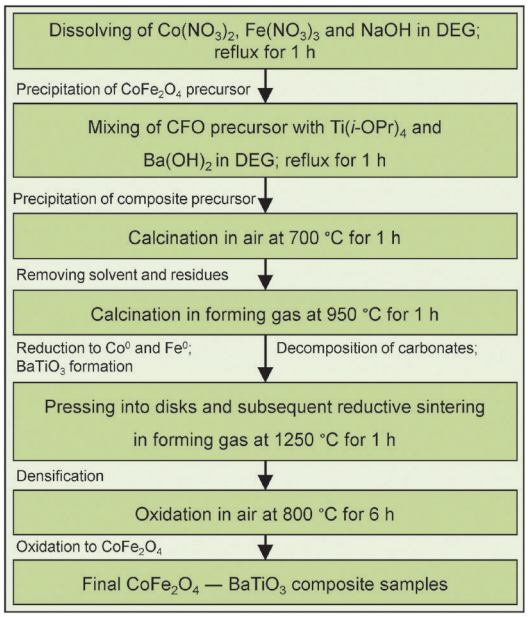

Fig. 1 Scheme of sample preparation.

composites were synthesized with x_{CFO} = 0.1, 0.2, 0.3, 0.4 and 0.5. A modified polyol mediated process was used to prepare the precursor powders for the ceramics.[23,24] The preparation scheme is shown in Fig. 1 and is described as follows.

$Fe(NO_3)_3{\cdot}9H_2O$ (20 mmol, Sigma Aldrich) and $Co(NO_3)_2{\cdot}6H_2O$ (10 mmol, Sigma Aldrich) were dissolved in deionized water (6 ml). NaOH (80 mmol, Grüssing) and diethylene glycol (250 ml, Carl Roth) were added to the red solution, which was then heated within 45 min to its boiling point (~160 °C) and refluxed for 1 h. After cooling to room temperature, acetone (250 ml, Overlack) was added, resulting in a brown precipitate. Subsequent centrifugation and washing with acetone led to a brown $CoFe_2O_4$ precursor powder. The amount of ferrite was determined by thermogravimetric analysis.

For sample 0.5CFO–0.5BTO, 5 mmol of the presynthesized $CoFe_2O_4$ precursor and 5 mmol $Ba(OH)_2{\cdot}8H_2O$ (FLUKA) were mixed with diethylene glycol (250 ml, Carl Roth) in an argon flushed flask. Distilled Ti(i-OPr)$_4$ (5 mmol, Alfa Aesar) was added and the reaction mixture was heated within 45 min to the boiling point (~160 °C) and kept under reflux for 1 h. After cooling to room temperature, 250 ml of acetone (Overlack) were added to the gray suspension and subsequent centrifugation and washing with acetone led to a gray composite precursor. The precursor powders for the other samples were prepared accordingly, using the respective stoichiometric quantities.

The precursor powders were first calcined in static air at 700 °C for 1 h with a heating rate of 10 K min^{-1}. Afterwards, a first reduction step in flowing forming gas (80 ml min^{-1}, 10% H_2) at 950 °C for 1 h (heating rate 5 K min^{-1}) was performed and the resulting light gray powders were pressed into disks (100 mg, ∅ = 6 mm) that were sintered in flowing forming gas (80 ml min^{-1}, 10% H_2) at 1250 °C for 1 h (heating rate 5 K min^{-1}). Finally, reoxidation in static air at 800 °C for 6 h (heating rate 10 K min^{-1}) led to black ceramic bodies of $CoFe_2O_4$–$BaTiO_3$ composites.

2.2 Characterization

Thermogravimetric measurements in flowing synthetic air or forming gas (10% H_2) (flow rate 40 ml min^{-1}, heat rate 10 K min^{-1}) were performed using a Netzsch STA 409 system. X-ray diffraction patterns were recorded at room temperature on a Bruker D8 Advance diffractometer operating with CuKα radiation. For the quantitative cobalt ferrite determination, small aliquots of the samples were dissolved in a mixture of hydrochloric acid (≥37%, Sigma Aldrich) and hydrogen peroxide solution (30%, Overlack). After dissolution, residual peroxides were decomposed by heating. The solutions were diluted to an approximated Fe concentration of 1 mg l^{-1} and Spectroquant Iron Test solution (Merck Millipore) was added. For absorbance measurements at λ = 560 nm a VWR UV-3100PC Spectrophotometer was used. The Fe concentrations and corresponding $CoFe_2O_4$ contents were determined by a calibration series. Scanning electron microscopy images in the backscattered electron (BSE) mode and EDX spectra were recorded using a Philips ESEM XL 30 FEG. For impedance measurements an eutectic Ga–In alloy was coated as electrodes on top and bottom surfaces of the ceramic bodies. The temperature and frequency dependent impedance spectra (0 to 180 °C; 100 Hz to 13 MHz) were recorded using a Hewlett-Packard 4192A impedance analyzer. Magnetic measurements were carried out using the ACMS option of a Quantum Design PPMS 9. Hysteresis loops were measured at 300 K with a cycling of the magnetic field between +90 and −90 kOe. For the magnetoelectric investigations, 100 nm thick gold electrodes were sputtered onto the sample surfaces using a Cressington Sputter Coater 108auto. Electric poling was done applying an electric DC field of 4 kV cm^{-1} to the samples at room temperature. Then the samples were heated to 200 °C for 1 h (heating rate 10 K min^{-1}) and the electric field was dynamically adjusted setting the current limit to 0.1 mA. Due to the increasing conductivity of the samples the field decreased to a few V cm^{-1} at 200 °C but again reached 4 kV cm^{-1} during cooling to room temperature. After poling, the samples were short circuited for 10 min. Immediately afterwards, the ME measurements were performed at 300 K in a Quantum Design PPMS 9 using a custom made setup based on the AC-Transport measurement option. A magnetic AC field of H_{ac} = 10 Oe with different frequencies was applied by a solenoid with 1160 loops of copper wire and the ME voltage was measured in dependence of the magnetic DC field upon cycling between +10 and −10 kOe. Magnetic AC and DC fields were aligned parallel to the electric polarization. Raw data were corrected for eddy currents measured on an empty sample holder. The magnetoelectric coefficient was calculated as $\alpha_{ME} = U/(H_{ac}{\cdot}h)$ with h being the sample height.

3. Results and discussion

3.1 Thermal analysis

Simultaneous thermogravimetric and differential thermal analyses were carried out on the samples to investigate calcination, sintering and reoxidation behavior. The results are discussed for 0.3CFO–0.7BTO exemplarily as follows.

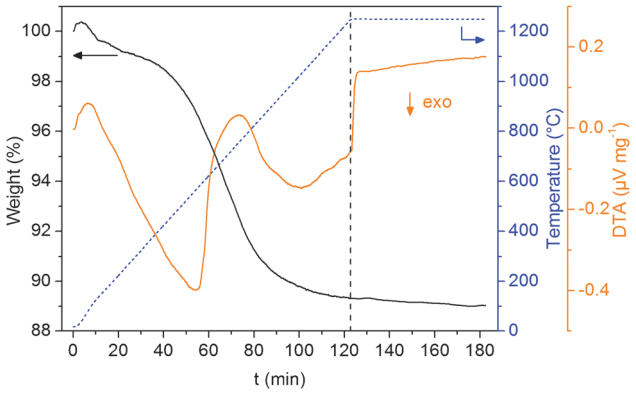

Fig. 2 TGA/DTA investigation of 0.3CFO–0.7BTO air-calcined powder under reductive sintering conditions in flowing forming gas.

Calcination of the dried composite precursor in air at 700 °C leads to a total weight loss of 45%. This weight change comprises the evaporation of residual solvent and adsorbed water, an exothermal combustion of organic residues and the endothermal decomposition of intermediately formed $BaO_x(CO_3)_{1-x}$.[25–27]

Following the path of preparation and representing the calcination and sintering steps under reducing conditions, an air-calcined sample was heated in the thermobalance in flowing forming gas to 1250 °C and kept at this temperature for 1 h. The corresponding weight change and DTA curves are shown in Fig. 2. The main weight loss of 9.0% occurs between 350 and 1000 °C and is accompanied by two distinct exothermal signals in the DTA curve. During this step, the reduction of $CoFe_2O_4$ to an alloy of Co and Fe (expected weight loss: 7.7%), the decomposition of residual $BaCO_3$ and the final formation of $BaTiO_3$ take place. During the dwell time of 1 h at 1250 °C a further slight weight loss of about 2% was observed. This weight loss could be caused by a gradual generation of oxygen defects and the accompanied partial reduction of Ti^{4+} in the $BaTiO_3$ matrix. Overall a weight loss of 11.0% occurred.

Afterwards, the resulting $CoFe_2$–$BaTiO_3$ sample was heated in synthetic air up to 800 °C and kept at that temperature for 6 h to investigate the reoxidation behavior. As shown in Fig. 3, a weight gain accompanied by an exothermic DTA signal starts at 430 °C and is finished about 1 h after reaching 800 °C. This process leads to a total weight change of +8.2%. Longer heating at 800 °C did not lead to any significant additional weight change. For the complete oxidation of the $CoFe_2$ alloy in the 0.3CFO–0.7BTO sample, a theoretical weight gain of 8.4% is expected. Thus, the observed change of +8.2% can be assigned completely to the reoxidation of the alloy to $CoFe_2O_4$ as additionally supported by the XRD results discussed in the next paragraph.

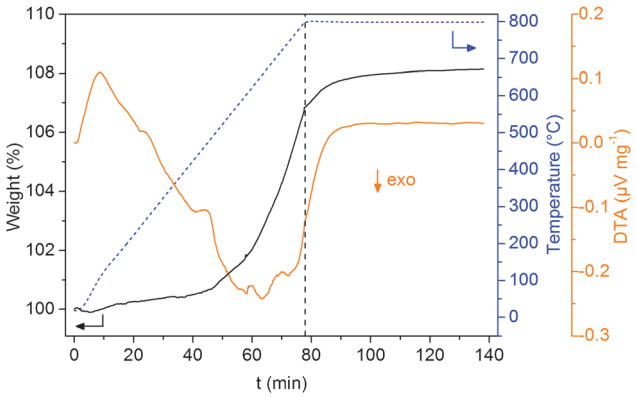

Fig. 3 TGA/DTA investigation in flowing air of 0.3$CoFe_2$–0.7BTO under reoxidation conditions.

3.2 X-ray diffraction

The course of the synthesis was monitored by X-ray powder diffraction as exemplarily shown for x_{CFO} = 0.5 in Fig. 4. The diffractogram of the precursor obtained by precipitation without further temperature treatment (Fig. 4a) mainly shows crystalline $BaCO_3$ and $CoFe_2O_4$ implying that at least one Ti-containing amorphous phase is present. Calcination in air at 700 °C for 1 h leads to the formation of $BaTiO_3$ although some $BaCO_3$ is still detectable in the powder (Fig. 4b). Calcination or sintering in air at temperatures higher than 700 °C leads to reactions between the $BaTiO_3$ matrix and the ferrite, *i.e.* the formation of impurities such as Ti^{4+}- and Co^{2+}-doped $BaFe_{12}O_{19}$, hexagonal $BaTiO_3$ as well as increased Co^{2+} and Fe^{3+} doping of $BaTiO_3$. To avoid this, an additional calcination step in forming gas (10% H_2) at 950 °C for 1 h was performed. Under these conditions residual $BaCO_3$ decomposes and the X-ray diffraction pattern (Fig. 4c) indicates the formation of (pseudo-) cubic modification for $BaTiO_3$. In addition, $CoFe_2O_4$ is reduced to an alloy of Co and Fe that does not react with $BaTiO_3$ as the ferrite would. The resulting reduced powder was pressed into disks (∅ = 6 mm, m = 100 mg) and sintered at 1250 °C for 1 h in forming gas. The corresponding X-ray diffraction pattern shows a mixture of tetragonal $BaTiO_3$ and the $CoFe_2$ alloy (Fig. 4d). Afterwards, the ceramic body was reoxidized in air at 800 °C for 6 h resulting in an oxidation of the $CoFe_2$ alloy to $CoFe_2O_4$ (Fig. 4e).

As shown in Fig. 5, phase pure $CoFe_2O_4$–$BaTiO_3$ composites were obtained for all investigated compositions with x_{CFO} = 0.1, 0.2, 0.3, 0.4, and 0.5. By Rietveld refinement the cell parameters

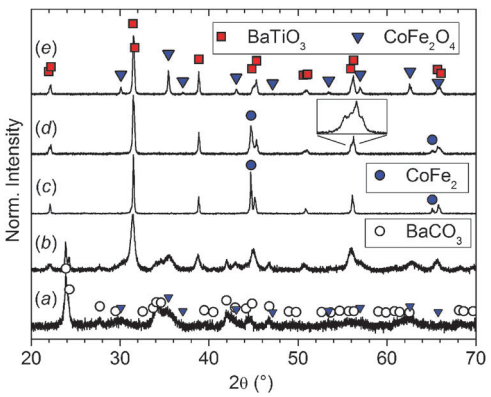

Fig. 4 X-ray diffraction patterns of 0.5CFO–0.5BTO: (a) precursor; (b) calcined in air at 700 °C for 1 h; (c) calcined in forming gas at 950 °C for 1 h; (d) sintered in forming gas at 1250 °C for 1 h, zoom: tetragonal splitting of $BaTiO_3$ 211 reflex; (e) reoxidized in air at 800 °C for 6 h.

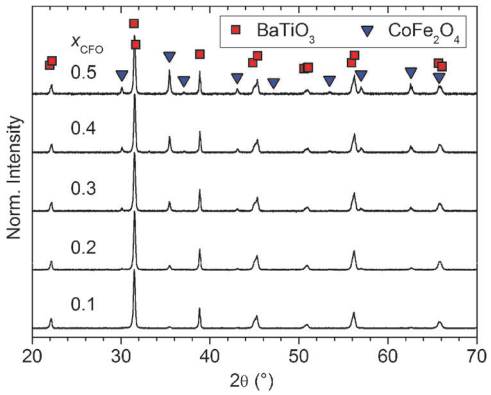

Fig. 5 X-ray diffraction patterns of composites with increasing $CoFe_2O_4$ content.

of the $BaTiO_3$ matrix were determined as a = 3.9997(6) and c = 4.0254(8) for all samples. Indicating a homogeneous composition independent of x_{CFO}. Thus, by reductive sintering and subsequent reoxidation, the formation of impurities as $BaFe_{12}O_{19}$ can be prevented completely and the reaction of $BaTiO_3$ with Co^{2+} and Fe^{3+} is minimized.

It was found that if the disks are too dense after the reductive sintering, the oxidation leads to cracks in the samples due to an increasing volume during the reaction of $CoFe_2$ to $CoFe_2O_4$. The optimal relative densities for reoxidizing (65 to 80%) are dependent on x_{CFO} and decrease with higher $CoFe_2O_4$ content. For the final samples relative densities, with respect to the (weighted) single crystal values,[28] between 80% and 90% were achieved.

3.3 Photometric $CoFe_2O_4$ assay

In Table 1 the results of the photometric $CoFe_2O_4$ quantifications are listed. The uniform deficiency in the $CoFe_2O_4$ content compared to the nominal values is most likely caused by a certain solubility of the Co- and Fe-containing precursors during precipitation and washing of the composite powder. On the other hand the deviation between the expected and measured $CoFe_2O_4$ content is below 2 mol% in most cases and for simplification the nominal percentages are used throughout the text for describing the compositions. Nevertheless, for all calculations with respect to x_{CFO}, the experimentally determined contents were used.

3.4 SEM and EDX investigations

Scanning electron micrographs were taken from the polished surfaces of sintered samples as shown exemplarily in Fig. 6 for x_{CFO} = 0.1, 0.3 and 0.5. A minor porosity was observed for all

Table 1 $CoFe_2O_4$ contents calculated from photometric iron analysis

	$CoFe_2O_4$ mole fraction (mol%)	
Sample	Nominal	Determined
0.1CFO–0.9BTO	10	8.7 ± 0.4
0.2CFO–0.8BTO	20	18.4 ± 0.5
0.3CFO–0.7BTO	30	28.2 ± 0.9
0.4CFO–0.6BTO	40	37.9 ± 1.4
0.5CFO–0.5BTO	50	46.3 ± 1.4

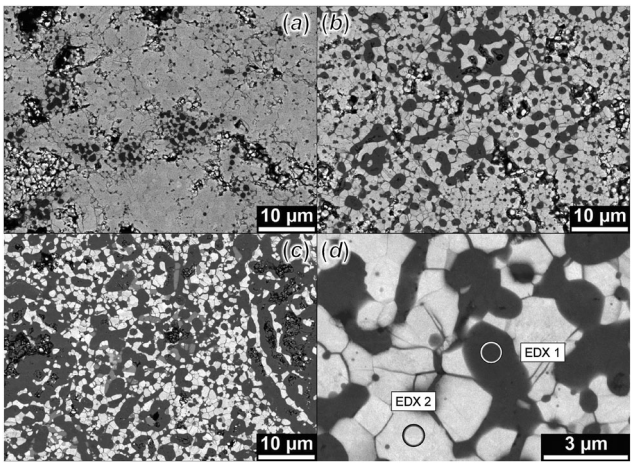

Fig. 6 Scanning electron microscopy images (BSE mode) of polished ceramics: (a) x_{CFO} = 0.1; (b) 0.3; (c) 0.5; (d) position markers for EDX spectra of 0.3CFO–0.7BTO, roughly representing the irradiated surface area.

samples in accordance with the measured densities of 80% to 90%. The pores are distributed randomly throughout the samples. The $BaTiO_3$ phase was found to consist of grains with sizes of 1–5 μm independent of x_{CFO}. From Fig. 6a it can be seen that for 0.1CFO–0.9BTO isolated $CoFe_2O_4$ grains (dark gray) are embedded in the $BaTiO_3$ matrix (light gray) but most of the $CoFe_2O_4$ is assembled in centers of partially interconnected grains separated and surrounded by $BaTiO_3$. With higher x_{CFO} values the amount of these $CoFe_2O_4$ clusters increases. In 0.3CFO–0.7BTO only a small portion of the ferrite occurs as isolated particles completely surrounded by $BaTiO_3$ (Fig. 6b and d). For x_{CFO} = 0.4 and 0.5 (Fig. 6c), the $CoFe_2O_4$ particles form irregular connected structures that permeate through wide areas, from several 10 to 100 μm in diameter.

To assign the two distinguishable phases in the BSE mode, EDX measurements were carried out at representative sample areas (Fig. 6d). The EDX spectra confirm the formation of two phases, namely $CoFe_2O_4$ and $BaTiO_3$, as can be seen in Fig. 7. The traces of barium and titanium, visible in the $CoFe_2O_4$ spectrum, are due to the large interaction volume of the electron beam compared to the grain size.

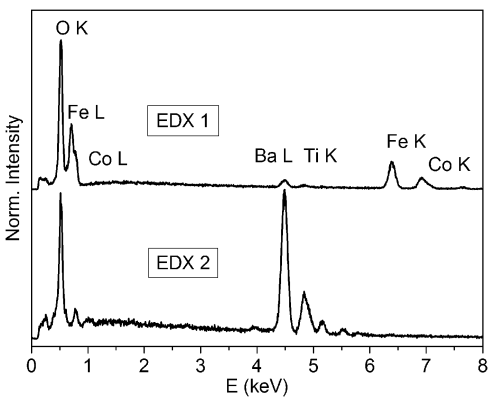

Fig. 7 EDX spectra of 0.3CFO–0.7BTO at the two positions marked in Fig. 6d.

In 0.5CFO–0.5BTO a third phase can be identified in the BSE images from its medium-gray contrast, although no additional reflexes show up in the corresponding X-ray diffraction pattern. EDX-line scans revealed this phase to be slightly oxygen-deficient $BaTiO_{3-\delta}$.

3.5 Impedance spectroscopy

In Fig. 8 the temperature dependence of the real part of the permittivities (ε') and the corresponding loss tangents measured at 1 kHz are shown. The ε' values at 0 °C vary between 476 for x_{CFO} = 0.1 and 232 for x_{CFO} = 0.5. In the measured temperature range the permittivities of x_{CFO} = 0.1 and 0.2 increase continuously, reaching 5610 and 5068 at 180 °C. For the composite with x_{CFO} = 0.3 the formation of a broad shoulder at around 150 °C can be seen and ε' reaches a value of about 4650 at 180 °C. For x_{CFO} = 0.4 and 0.5, a maximum forms at 150 °C with ε' values of 4402 and 4447. When measured at frequencies higher than 10 kHz, this maximum at 150 °C is also observed for the samples 0.1CFO–0.9BTO and 0.2CFO–0.8BTO as shown in Fig. 9 for f = 1 MHz. The occurrence of the maximum is accompanied by an increase in the loss tangent and can be assigned to the ferroelectric–paraelectric transition of $BaTiO_3$.[29–32] For large-grained $BaTiO_3$ this phase transition occurs at 120 °C.

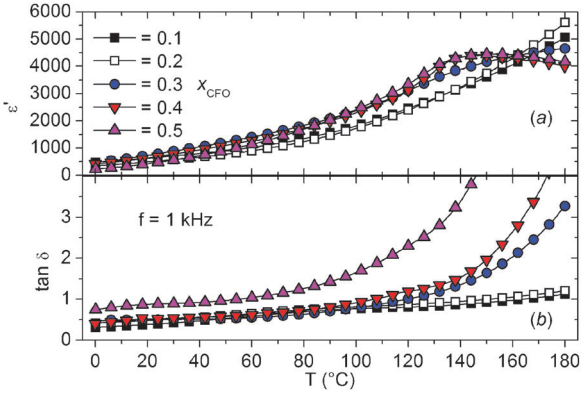

Fig. 8 (a) Temperature dependence of the real part of the permittivity and (b) corresponding loss tangents at 1 kHz.

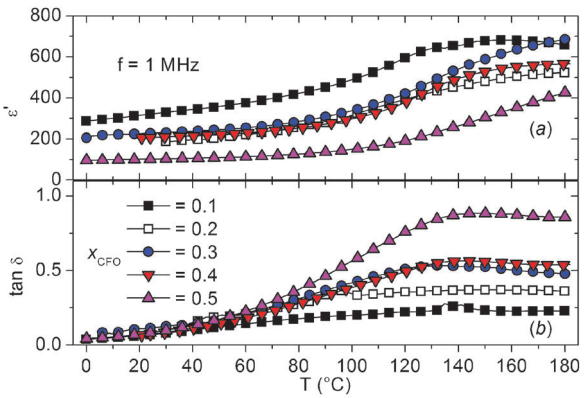

Fig. 9 (a) Temperature dependence of the real part of the permittivity and (b) corresponding loss tangents at 1 MHz.

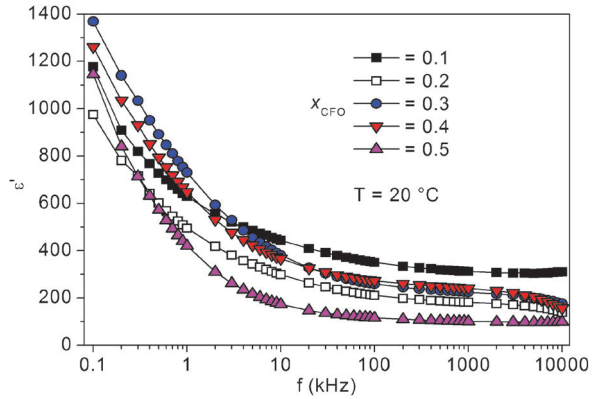

Fig. 10 Frequency dependence of the real part of the permittivities at room temperature.

According to Mitoseriu *et al.* the shift to 150 °C is due to the convolution of extrinsic defect-related dielectric relaxation with the intrinsic ferroelectric component.[33] The presence of the phase transition in the impedance data proves the formation of the tetragonal (ferroelectric) $BaTiO_3$ modification in accordance with the XRD results discussed above. The consistent phase transition temperatures hint at a uniform composition of the $BaTiO_3$, indicating that no x_{CFO}-dependent doping of Co^{2+} or Fe^{3+} occurred for any of the samples. The loss tangents at room temperature are below 0.5 with the exception of 0.5CFO–0.5BTO and only slightly increase with temperature below the tetragonal–cubic phase transition of $BaTiO_3$.

Concerning the frequency dependence at room temperature, ε' decreases rather strongly in the range of roughly 100 Hz–10 kHz and remains quite stable for higher frequencies for all samples, as can be seen in Fig. 10. This phenomenon is typical for electrically conducting particles embedded in an insulating matrix and is called Maxwell Wagner polarization.[34] A similar behavior has already been reported for various $CoFe_2O_4$–$BaTiO_3$ composites.[13,35,36]

3.6 Magnetic properties

The field dependent magnetization curves of the composites are depicted in Fig. 11. All samples show clear hystereses in accordance with the ferrimagnetism of the spinel component. The saturation magnetization values were determined by a linear extrapolation of the magnetization in the high field ranges (50–90 kOe) to H = 0 Oe. As expected, saturation and remanent magnetization increase with $CoFe_2O_4$ content.

Normalizing these magnetization values with respect to the ferrite content (*i.e.* emu g^{-1} of $CoFe_2O_4$), as shown in Fig. 12, reveals a small maximum of M_R with a value of 27.0 emu g^{-1} for x_{CFO} = 0.3, while the M_S data show a general slight increase with higher $CoFe_2O_4$ contents, reflecting the increasing ferrite particle sizes. Coercivity fields increase from 1060 Oe (0.1CFO–0.9BTO) to a maximum of 1230 Oe for x_{CFO} = 0.2 and decreases with higher $CoFe_2O_4$ contents down to a minimum of 970 Oe for x_{CFO} = 0.5. It is commonly known that coercivity values for $CoFe_2O_4$ are dependent on its grain shape and structure. Therefore, the change in coercivity is probably due

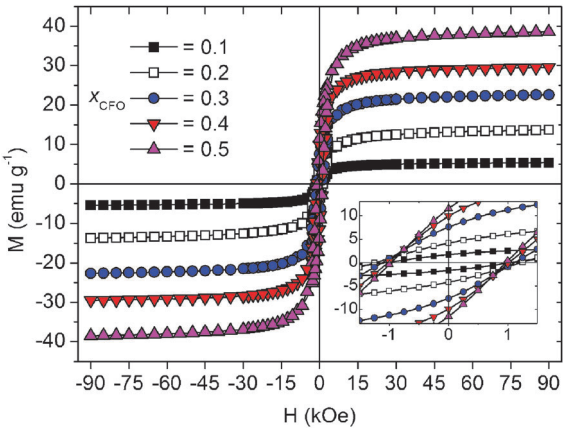

Fig. 11 Field dependent magnetization hysteresis curves measured at 300 K. The inset shows a magnification of the low field region.

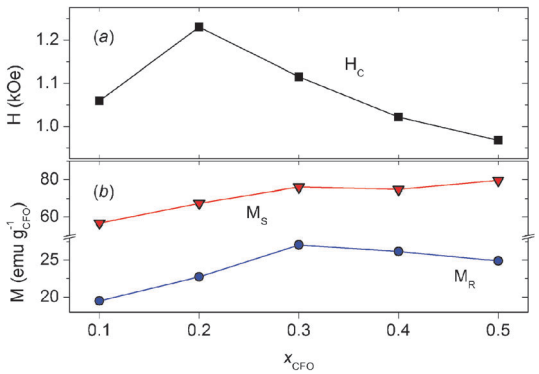

Fig. 12 (a) Magnetic coercive fields and (b) saturation and remanent magnetization at 300 K.

to the formation of $CoFe_2O_4$ clusters and interconnected structures with increasing x_{CFO} values (see SEM part).

3.7 Magnetoelectric coupling

An example of the magnetic DC field dependence of the magnetoelectric coefficient α_{ME} is shown in Fig. 13 for the composite with x_{CFO} = 0.4. For all samples, the α_{ME} values show maxima/minima around ±2.5 kOe and clear hysteretic behavior with coercive fields between ±400 and ±600 Oe as well as distinct remanent α_{ME} values of ±7 to ±150 μV Oe^{-1} cm^{-1}. Thus, the sign of α_{ME} is switchable with the direction of the applied magnetic DC field.

It is remarkable that the maximum values of α_{ME} at ±2.5 kOe are dependent on the history of the magnetic DC field. Upon increasing the DC field strength (both in positive and negative direction), the α_{ME} values are higher than for decreasing field strengths. For example, in the case of x_{CFO} = 0.4 the maximum α_{ME} value is 420 μV Oe^{-1} cm^{-1} when the magnetic field is increased up to 10 kOe (red circles, Fig. 13), whereas $\alpha_{ME(max)}$ amounts to only 337 μV Oe^{-1} cm^{-1} when the field strength is lowered down from 10 kOe (blue diamonds, Fig. 13). To the best of our knowledge, such an effect has not yet been described for α_{ME} and its origin needs to be investigated in further experiments.

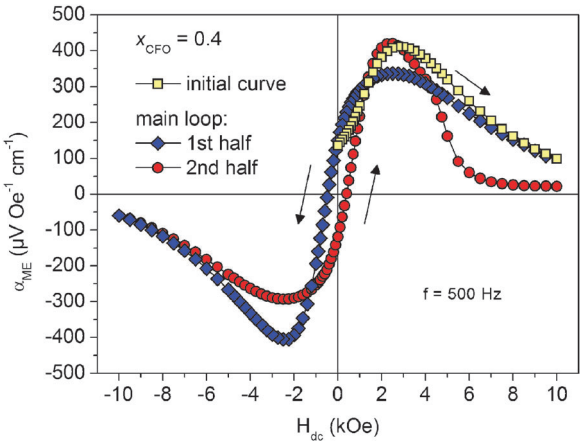

Fig. 13 Magnetic DC field dependent magnetoelectric coefficient of 0.4CFO–0.6BTO.

A comparison between the magnetic and ME hystereses (Fig. 14) reveals that the ME coercivities are about half the size of the magnetic coercivites, *i.e.* the ME voltage diminishes although magnetization still exists. It is noteworthy that the DC field at which the maximum α_{ME} is ovserved (±2.5 kOe) shows no obvious relation to the characteristic points of the magnetic hysteresis. In particular, it is much smaller than the saturation field (roughly ±20 kOe) and also significantly different from the inflection points of magnetization which occur at about ±1 kOe. It seems that the ME effect is more affected by magnetostriction. For example, van Run *et al.* found the highest ME values at the maximum of the piezomagnetic strain per Oe.[37] In laminated PZT–Terfenol-D systems, ME maxima were found at the saturation point of the magnetostrictive strain[38] and at the maximum of the piezomagnetic coefficient.[39]

Our paper is one of the few examples in which a hysteretic behavior of the ME coefficient is reported for $CoFe_2O_4$–$BaTiO_3$ composites.[37,40–43] In the majority of articles (*e.g.* ref. 13 and 44–47), α_{ME} values were found to be zero when the magnetic DC field was switched off, or only initial curves, *i.e.* without cycling of H_{dc}, were published.

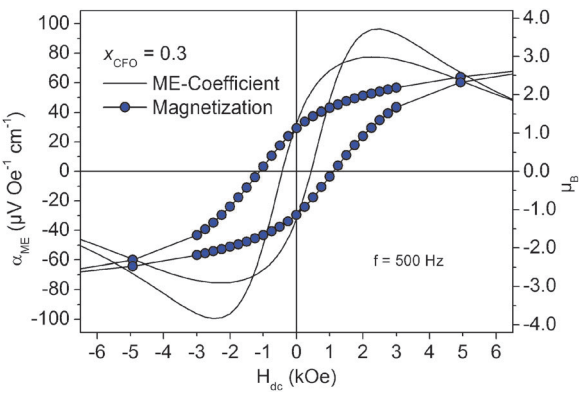

Fig. 14 Comparison of magnetic and magnetoelectric hystereses of 0.3CFO–0.7BTO.

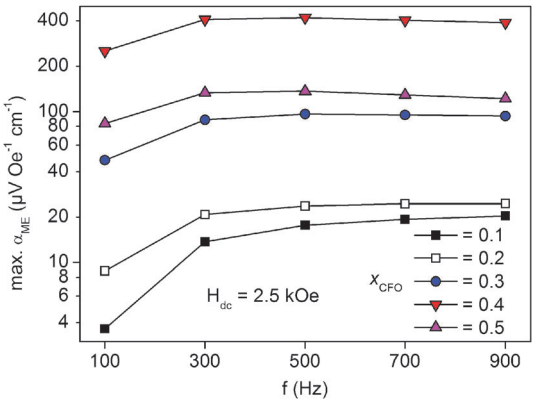

Fig. 15 Frequency dependence (H_{ac}) of the maximal ME coefficients.

Fig. 15 shows the maximum α_{ME} values for the investigated samples depending on x_{CFO} and the frequency of H_{ac}. The α_{ME} values increase with higher $CoFe_2O_4$ contents up to a maximum at x_{CFO} = 0.4 with 420 μV Oe^{-1} cm^{-1} at 500 Hz and decrease again for x_{CFO} = 0.5 at all investigated frequencies. The magnetoelectric remanences follow this trend and the sample 0.4CFO–0.6BTO shows the highest remanent α_{ME} value with 150 μV Oe^{-1} cm^{-1}. The maximum α_{ME} values are within the typical range of a few μV Oe^{-1} cm^{-1} to some mV Oe^{-1} cm^{-1} reported for $CoFe_2O_4$–$BaTiO_3$ composites with 0–3 connectivity measured under similar conditions.[13–15,41,43]

ME measurements at five different H_{ac} frequencies showed that α_{ME} is significantly lower for f = 100 Hz than for higher frequencies, while for frequencies from 300 to 900 Hz the obtained α_{ME} values show only little deviations. This is in contrast to previously reported frequency dependencies where α_{ME} values increase more or less linearly up to 1 kHz.[44,45] Other articles show a giant increase of α_{ME} (up to 2.5 V Oe^{-1} cm^{-1}) under resonance conditions in the range between 15 and 430 kHz.[46–48] Measurements at such higher frequencies are therefore planned for the future.

4. Conclusions

In multiferroic composites, the strength of the magnetoelectric coupling depends on the quality of the interface and therefore an intimate contact between the two components is mandatory. Because of the low sintering activity of $BaTiO_3$, such high-quality interfaces require high sintering temperatures, which usually lead to the formation of secondary phases like $BaFe_{12}O_{19}$ and/or ionic exchanges like the incorporation of iron or cobalt ions in $BaTiO_3$. To avoid these problems we describe a new approach starting with the polyol-assisted soft-chemistry preparation of a $CoFe_2O_4$–$BaTiO_3$ composite precursor consisting of submicrometer-sized particles. This composite powder is sintered under a reducing atmosphere, resulting in $CoFe_2$–$BaTiO_3$ composites. In a final reaction step these ceramics are reoxidized under mild conditions leading to the final dense $CoFe_2O_4$–$BaTiO_3$ composites (≥80% of the crystallographic density), which according to XRD are completely free of secondary phases. The presence of tetragonal $BaTiO_3$ with lattice parameters independent of the ferrite fraction further indicates that no considerable amounts of Co^{2+} or Fe^{3+} are incorporated in $BaTiO_3$. This finding is additionally corroborated by dielectric measurements showing the occurrence of the ferroelectric–paraelectric phase transition, which is shifted to 150 °C probably due to defect-related dielectric relaxations. EDX investigations gave no hints for secondary phases or detectable Ti/Fe/Co exchange between the two phases. All composites show ferrimagnetic behavior. Their (normalized) saturation magnetizations slightly increase with the $CoFe_2O_4$ content, reflecting the increasing grain sizes of the ferrite. Field-dependent measurements of the magnetoelectric coupling show a hysteresis of α_{ME} with maxima at DC magnetic fields of ±2.5 kOe and remanent α_{ME} values in the order of 10–150 μV Oe^{-1} cm^{-1}. We observed distinct deviations between the coercivities of the magnetic moment and the ME effect, *i.e.* the magnetoelectric coupling diminishes already at roughly ±500 Oe while the required field to extinct the magnetization is about twice as high. Concerning the effect of the H_{ac} frequency, we found almost constant α_{ME} values from 300 Hz to 900 Hz while the magnetoelectric coupling is much smaller at 100 Hz. In addition, an increase of the ME effect with increasing $CoFe_2O_4$ content was observed leading to a maximum in the order of 400 μV Oe^{-1} cm^{-1} for x = 0.4. With a higher ferrite content, α_{ME} decreases again. Most interestingly, for all samples we observed strong differences for the maximum α_{ME} values depending on the direction of the magnetic dc-field sweep. When the field strength is increased (both in positive and negative directions) the maximum ME values are up to 20% larger than upon decreasing H_{dc}. Thus, the measured ME voltages of the $CoFe_2O_4$–$BaTiO_3$ composites not only depend on the H_{dc} field strength but also on its history. This 'memory effect' may give rise to additional future applications.

Acknowledgements

The authors thank F. Syrowatka for the SEM investigations and Th. Müller for TGA experiments. Financial support by the German Research Foundation within the Collaborative Research Centre SFB 762 *Functionality of Oxide Interfaces* is gratefully acknowledged.

References

1 N. A. Spaldin and M. Fiebig, *Science*, 2005, **309**, 391–392.
2 M. Bibes and A. Barthélémy, *Nat. Mater.*, 2008, **7**, 425–426.
3 J. Ma, J. Hu, Z. Li and C.-W. Nan, *Adv. Mater.*, 2011, **23**, 1062–1087.
4 N. Ortega, A. Kumar, J. F. Scott and R. S. Katiyar, *J. Phys.: Condens. Matter*, 2015, **27**, 504002.
5 W. Eerenstein, N. D. Mathur and J. F. Scott, *Nature*, 2006, **442**, 759–765.
6 J. van den Boomgaard, D. R. Terrell, R. A. J. Born and H. F. J. I. Giller, *J. Mater. Sci.*, 1974, **9**, 1705–1709.
7 C.-W. Nan, *Phys. Rev. B: Condens. Matter Mater. Phys.*, 1994, **50**, 6082–6088.

8 M. Avellaneda and G. Harshé, *J. Intell. Mater. Syst. Struct.*, 1994, **5**, 501–513.
9 M. I. Bichurin, V. M. Petrov and G. Srinivasan, *J. Appl. Phys.*, 2002, **92**, 7681–7683.
10 J. Ryu, S. Priya, K. Uchino and H.-E. Kim, *J. Electroceram.*, 2002, **8**, 107–119.
11 R. E. Newnham, D. P. Skinner and L. E. Cross, *Mater. Res. Bull.*, 1978, **13**, 525–536.
12 C.-W. Nan, M. I. Bichurin, S. Dong, D. Viehland and G. Srinivasan, *J. Appl. Phys.*, 2008, **103**, 031101.
13 R. P. Mahajan, K. K. Patankar, M. B. Kothale, S. C. Chaudhari, V. L. Mathe and S. A. Patil, *Pramana*, 2002, **58**, 1115–1124.
14 G. Schileo, *Prog. Solid State Chem.*, 2013, **41**, 87–98.
15 A. Baji, Y.-W. Mai, R. Yimnirun and S. Unruan, *RSC Adv.*, 2014, **4**, 55217–55223.
16 J. S. Andrew, J. D. Starr and M. A. K. Budi, *Scr. Mater.*, 2014, **74**, 38–43.
17 X. Chen and G. Tan, 2012, arXiv:1201.3963 [cond-mat.mtrl-sci].
18 T. Kimura, *Annu. Rev. Condens. Matter Phys.*, 2012, **3**, 93–110.
19 Z. Dong, Y. Pu, Z. Gao, P. Wang, X. Liu and Z. Sun, *J. Eur. Ceram. Soc.*, 2015, **35**, 3513–3520.
20 J. D. S. Guerra, S. Betal, M. Pal, J. E. Garcia, A. J. A. Oliveira, J.-C. M'Peko, A. C. Hernandes, R. Guo and A. S. Bhalla, *J. Am. Ceram. Soc.*, 2015, **98**, 1542–1547.
21 N. Koga and T. Tsutaoka, *J. Magn. Magn. Mater.*, 2007, **313**, 168–175.
22 T. Tsutaoka and N. Koga, *J. Magn. Magn. Mater.*, 2013, **325**, 36–41.
23 D. Caruntu, Y. Remond, N. H. Chou, M.-J. Jun, G. Caruntu, J. He, G. Goloverda, C. O'Connor and V. Kolesnichenko, *Inorg. Chem.*, 2002, **41**, 6137–6146.
24 M. Siemons, T. Weirich, J. Mayer and U. Simon, *Z. Anorg. Allg. Chem.*, 2004, **630**, 2083–2089.
25 S. Gablenz, H.-P. Abicht, E. Pippel, O. Lichtenberger and J. Woltersdorf, *J. Eur. Ceram. Soc.*, 2000, **20**, 1053–1060.
26 V. Ischenko, E. Pippel, R. Köferstein, H.-P. Abicht and J. Woltersdorf, *Solid State Sci.*, 2007, **9**, 21–26.
27 V. Ischenko, J. Woltersdorf, E. Pippel, R. Köferstein and H.-P. Abicht, *Solid State Sci.*, 2007, **9**, 303–309.
28 G. W. Marks and L. A. Monson, *Ind. Eng. Chem.*, 1955, **47**, 1611–1620.
29 A. Hanumaiah, T. Bhimasankaram, S. V. Suryanarayana and G. S. Kumar, *Bull. Mater. Sci.*, 1994, **17**, 405–409.
30 K. Raidongia, A. Nag, A. Sundaresan and C. N. R. Rao, *Appl. Phys. Lett.*, 2010, **97**, 062904.
31 A. Gupta and R. Chatterjee, *J. Eur. Ceram. Soc.*, 2013, **33**, 1017–1022.
32 R. Köferstein and S. G. Ebbinghaus, *RSC Adv.*, 2015, **5**, 71491–71499.
33 L. Mitoseriu and V. Buscaglia, *Phase Transitions*, 2006, **79**, 1095–1121.
34 K. W. Wagner, *Arch. Elektrotech.*, 1914, **2**, 371–387.
35 J. Nie, G. Xu, Y. Yang and C. Cheng, *Mater. Chem. Phys.*, 2009, **115**, 400–403.
36 L. M. Hrib and O. F. Caltun, *J. Alloys Compd.*, 2011, **509**, 6644–6648.
37 A. M. J. G. van Run, D. R. Terrell and J. H. Scholing, *J. Mater. Sci.*, 1974, **9**, 1710–1714.
38 S. Dong, J.-F. Li and D. Viehland, *J. Appl. Phys.*, 2004, **95**, 2625–2630.
39 C. P. Zhao, F. Fang and W. Yang, *Smart Mater. Struct.*, 2010, **19**, 125004.
40 J. van den Boomgaard, A. M. J. G. Van Run and J. Van Suchtelen, *Ferroelectrics*, 1976, **10**, 295–298.
41 M. E. Botello-Zubiate, D. Bueno-Baqués, J. de Frutos Vaquerizo, L. E. Fuentes Cobas and J. A. Matutes-Aquino, *Ferroelectrics*, 2006, **338**, 247–253.
42 G. V. Duong, R. Groessinger and R. Sato Turtelli, *J. Magn. Magn. Mater.*, 2007, **310**, 1157–1159.
43 G. V. Duong, R. S. Turtelli and R. Groessinger, *J. Magn. Magn. Mater.*, 2010, **322**, 1581–1584.
44 A. Khamkongkaeo, P. Jantaratana, C. Sirisathitkul, T. Yamwong and S. Maensiri, *Trans. Nonferrous Met. Soc. China*, 2011, **21**, 2438–2442.
45 H. Yang, G. Zhang and Y. Lin, *J. Alloys Compd.*, 2015, **644**, 390–397.
46 W. P. Wang, H. Yang, T. Xian and R. C. Yu, *Chem. Phys. Lett.*, 2015, **618**, 72–77.
47 R. A. Islam, M. Bichurin and S. Priya, in *Ferroelectrics – Characterization and Modeling*, ed. M. Lallart, InTech, 2011, pp. 61–78.
48 S. Q. Ren, L. Q. Weng, S.-H. Song, F. Li, J. G. Wan and M. Zeng, *J. Mater. Sci.*, 2005, **40**, 4375–4378.